Spectral behaviour of bismuth centres in different steps of the FCVD process

A.S. Zlenko, V.M. Mashinsky, L.D. Iskhakova, R.P. Ermakov, S.L. Semjonov, V.V. Koltashev

Abstract. **The behaviour of bismuth ions in silica glass free of other dopants has been studied in different steps of the furnace chemical vapour deposition (FCVD) process. Porous layers annealed and consolidated in different atmospheres, a bismuth chloride solution in acetone for porous layer impregnation, the resultant glass preform and holey fibres drawn out under various conditions have been characterised by spectroscopic techniques and X-ray diffraction. Active bismuth centres present in the preform and luminescing in the visible and IR spectral regions persist during drawing under reducing conditions, whereas drawing under oxidising conditions eliminates such centres. Annealing under reducing conditions produces absorption bands of IR-emitting bismuth centres (IRBCs) in spectra of fibres drawn out under oxidising conditions and concurrently increases the background loss. Under the annealing conditions of this study (argon atmosphere, $T_{max} = 1100\,°C$, 30 min), the IRBC concentration reaches a maximum and then decreases, whereas the background loss increases monotonically.**

1. Introduction

Bismuth-doped silica fibres with various core compositions ($Bi:Al_2O_3:SiO_2$, $Bi:GeO_2:SiO_2$, $Bi:P_2O_5:SiO_2$) enable lasing in the range 1140–1550 nm [1–7] and are thus potentially attractive as gain media for optical amplifiers in optical fibre communication systems [8]. Unfortunately, the physical nature of IR-emitting bismuth centres (IRBCs) is still unclear. A large number of hypotheses and models have been put forwards (see e.g. a review by Peng et al. [9]), but none has been confirmed. The problem is difficult to solve because the spectroscopic properties of bismuth centres strongly depend on glass composition and glass preparation conditions. It is, therefore, of interest to investigate in detail both the simplest system $Bi:SiO_2$ and the behaviour of bismuth in different steps of the fibre fabrication process, i.e. its transitions to states differing in properties. In this paper, we present a detailed experimental study of the behaviour of bismuth ions in silica glass free of other dopants in different steps of the furnace chemical vapour deposition (FCVD) process [10, 11] (a modification of

A.S. Zlenko, V.M. Mashinsky, L.D. Iskhakova, R.P. Ermakov, S.L. Semjonov, V.V. Koltashev Fiber Optics Research Center, Russian Academy of Sciences, ul. Vavilova 38, 119333 Moscow, Russia; e-mail: aszlenko@fo.gpi.ru

MCVD that uses a furnace instead of a burner). Such glass has been the subject of several studies [12–18]. This paper presents a continuation of previous work [17]. We report a spectroscopic study of a doping solution used for porous layer impregnation, the porous layers annealed and consolidated in different atmospheres, the resultant bismuth-doped glass preform and the fibre drawn out from the preform.

2. Spectroscopic properties of a bismuth(III) chloride solution in acetone

To dope fibre preforms with bismuth, a porous layer was impregnated with a solution of bismuth chloride, $BiCl_3$, in acetone, $CH_3–C(O)–CH_3$. It is worth noting that the proposed use of acetone as a solvent offers a number of advantages in comparison to acids: acetone is less hazardous, has lower viscosity, thereby enabling more rapid porous layer impregnation, vaporises considerably more rapidly and, hence, ensures a drastic reduction in porous layer drying time after the impregnation step.

Under excitation with the 337-nm nitrogen laser line, the starting colourless crystalline bismuth(III) chloride powder showed weak blue luminescence (which was probably due to the Bi^{3+} ion). Short-term exposure (1–2 min, ~1 W cm^{-2}) produced a black spot in the irradiated zone. Bismuth(III) chloride is known to experience photodissociation under UV irradiation (at 365 nm or shorter wavelengths [19]), which obviously took place in our case. Note that, after the darkening, there was no $BiCl_3$ luminescence.

With increasing bismuth chloride concentration in acetone, the colour of the solution changed from yellow to dark brown, almost black. After acetone vaporisation from the solution at room temperature, the tube contained black tarry substance, which obviously resulted from the reaction between the bismuth chloride and acetone. No reaction of $BiCl_3$ with acetone has been described in the literature. According to Sanderson and Bayse [20], bismuth halides may cause aldol condensation in ketones (bismuth halides can act as catalysts) and other nucleophilic additions to the C=O bond (BiX_3 interacts with the lone electron pair of the carbonyl oxygen, O_{CO}, increasing the positive charge on the carbon). Nevertheless, it is not yet clear what substances result from the reaction between $BiCl_3$ and acetone. In what follows, the reaction products will be denoted as $CH_3–C(O)–CH_3·BiCl_3$ [20]. That $BiCl_3$ reacted with acetone rather than just catalysing aldol self-condensation of acetone is further supported by the fact that the Raman spectrum of $BiCl_3$ differs drastically from that of the black substance (Fig. 1).

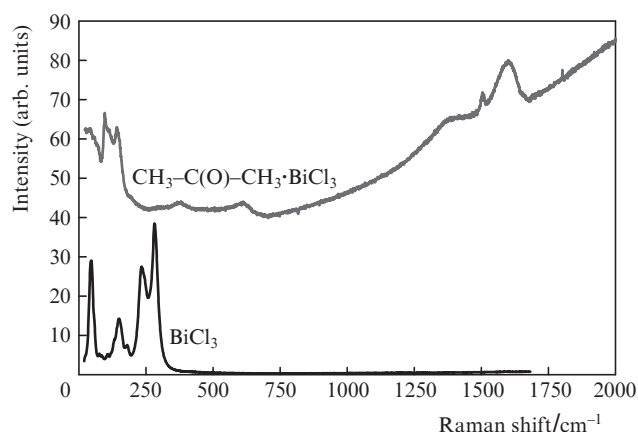$CH_3–C(O)–CH_3·BiCl_3$ was characterised by X-ray microanalysis. Its chemical composition was determined using a

Figure 1. Raman spectra of CH_3–$C(O)$–$CH_3 \cdot BiCl_3$ and $BiCl_3$.

JEOL JSM-5910LV scanning electron microscope (SEM) equipped with an Oxford Instruments energy dispersive X-ray spectrometer system. An SEM specimen was prepared as follows: a 5% $BiCl_3$ solution in acetone was applied to a quartz glass substrate and the solvent was evaporated. The backscattered electron (Z-contrast) images in Fig. 2 demonstrate that the specimen is rather inhomogeneous, with relatively large regions (200–600 µm in linear dimensions, Fig. 2a) differing markedly in average bismuth concentration. (The points and regions where the bismuth concentration was measured are indicated in Figs 2a–2d.) The micrographs in Figs 2c–2g, obtained at higher magnifications, indicate that the relatively large regions in Fig. 2a (similar in average bismuth concentration) are also inhomogeneous. At the highest magnification (Fig. 2g), we observe spherical particles ∼500 nm
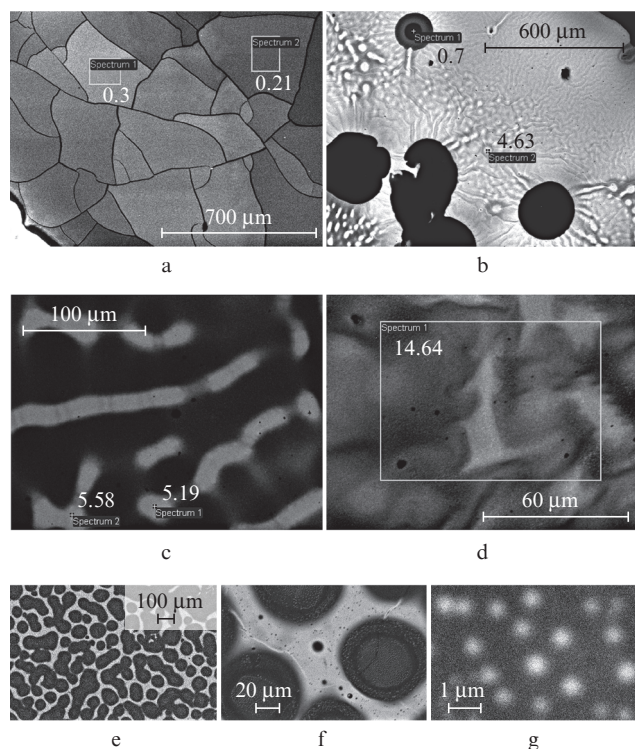
in size, in which the Bi : Cl atomic ratio is 1 : 3. Given the presence of such particles and the fact that the black substance was amorphous as determined by X-ray diffraction (XRD) (D8 Discover diffractometer with a GADDS, CuK_α radiation, graphite monochromator), it is reasonable to assume that $BiCl_3$ molecules enter into the composition of one of the reaction products without decomposition.

Figure 3 shows absorption spectra of $BiCl_3$ solutions in acetone at different $BiCl_3$ concentrations. Each absorption spectrum was obtained by subtracting the transmission spectrum of the $BiCl_3$ solution in acetone from that of pure acetone and normalising the difference by the thickness of the cuvette. The spectra are seen to contain strong UV absorption bands peaking at 230 and 330 nm. In the visible range, the spectra contain relatively weak absorption bands near 500 and 650 nm. The luminescence spectrum in Fig. 3b has the form of a broad band, 190 nm in width, peaking at 500 nm. The luminescence lifetime is ∼0.9 µs. No IR luminescence (1000–1750 nm) was detected under excitation at 337 or 975 nm. All the luminescence spectra presented in this paper were measured at room temperature with an Ando AQ-6315A optical spectrum analyser, unless otherwise indicated. No photochemical reaction was detected in the solution, and the luminescence intensity remained constant during the measurements. The luminescence spectrum of CH_3–$C(O)$–$CH_3 \cdot BiCl_3$ was identical to that of the solution. Thus, we are led to conclude that neither the solution nor the black substance contained IRBCs.
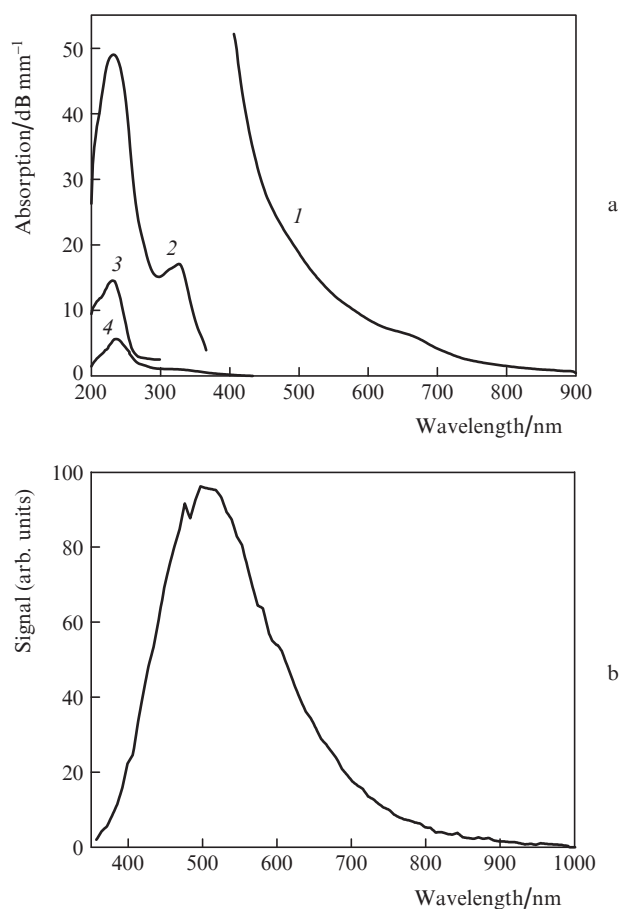

Figure 2. SEM micrographs of CH_3–$C(O)$–$CH_3 \cdot BiCl_3$. The numbers at indicated points and regions specify the atomic percentage of bismuth.

Figure 3. (a) Absorption spectra of $BiCl_3$ solutions in acetone: (1) 5, (2) 0.04, (3) 0.008 and (4) 0.001 wt% $BiCl_3$. (b) Luminescence spectrum of the solution containing 5 wt% $BiCl_3$ (excitation at $\lambda = 337$ nm).

3. Spectroscopic characterisation of porous layers annealed and consolidated in different atmospheres and at different temperatures

We fabricated several similar bulk samples in the form of 20-mm-diameter silica tubes of the same length, with an ~300-μm-thick porous layer produced on their inner surface by the FCVD process (Fig. 4b). The samples were impregnated with a $BiCl_3$ solution in acetone and then held at room temperature until the solvent vaporised. Next, the samples were heat-treated under various conditions and their luminescence and absorption were investigated.
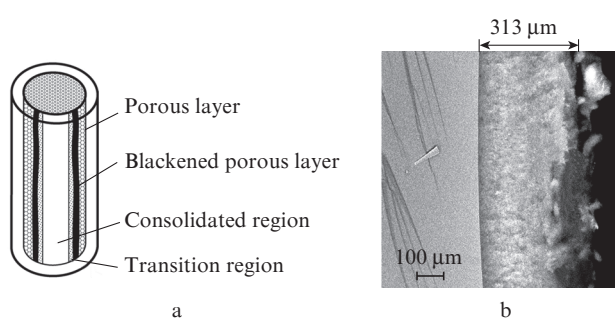

Figure 4. (a) Sample in which part of the porous layer was consolidated in air. (b) SEM micrograph of the interface between the porous layer and silica tube. The thickness of the porous layer is approximately 313 μm.

Annealing of impregnated samples at 1000, 1200 and 1400 °C for 1 h in air. Samples impregnated once with a 5% $BiCl_3$ solution in acetone were furnace annealed in air. This heat treatment failed to ensure porous layer consolidation. The annealed and unannealed (impregnated) samples had identical luminescence properties. No IR luminescence was detected under excitation in the ultraviolet (337 nm), visible (454, 488, 514, 567, 647, 676 nm) or infrared (975, 1064 nm) spectral region. Thus, bismuth does not form IR-emitting centres in silica glass under the conditions in question. At an excitation wavelength of 337 nm, the samples showed weak luminescence characteristic of $CH_3–C(O)–CH_3 \cdot BiCl_3$ (Fig. 3). Its intensity was considerably higher before annealing. In addition, annealing changed the colour of the impregnated porous layers from light brown to white. This is attributable to both the oxidation and partial vaporisation of $CH_3–C(O)–CH_3 \cdot BiCl_3$ during heating in air. The annealed samples were characterised by XRD and no crystalline bismuth compounds were detected.

Partial sintering of the porous layer in air. A sample was impregnated three times with a 5% $BiCl_3$ solution in acetone. After solvent vaporisation, part of the porous layer in the form of a thin bar along the tube (Fig. 4) was consolidated in air at 1900 °C using an oxygen–propane torch.

Heating converted the porous layer into ~60-μm-thick glass with a yellow tinge. In the immediate vicinity (on both sides) of the consolidated region, the upper surface (exposed to air) of the porous layer (~3 mm in width) blackened (Fig. 4a). According to XRD data, the porous layer darkened by heat treatment contained metallic bismuth crystals (Fig. 5). The crystallite size was ~20 nm as evaluated using the Scherrer formula. It is worth emphasising that it was the surface of the porous layer that blackened, whereas its interior remained white (as was seen on a fracture surface). This can be accounted for by bismuth vaporisation during sintering of the porous layer

and bismuth deposition (through the thermophoresis process) in the form of metallic bismuth crystals in a nearby region. The above experimental data demonstrate that the consolidation of the impregnated porous layer and collapse of the tube in the fibre preform fabrication process are accompanied by constant bismuth vaporisation and deposition, so that preforms with a uniform longitudinal bismuth profile may be difficult to produce.
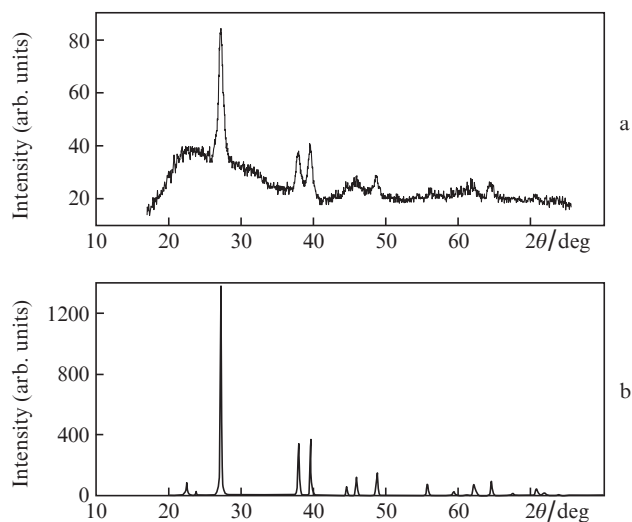

Figure 5. Comparison of the XRD patterns of (a) the porous layer and (b) metallic bismuth (ICDD, card no. 44-1246).

Figure 6 shows micrographs of various regions in the sample represented in Fig. 4a, which demonstrate how heat treatment changes their microstructure and the bismuth profile. Figure 6a shows an interfacial region between the porous layer (Fig. 6b) and transition region. It follows from Figs 6a and 6c–6e that the transition region is a porous layer, with bismuth-doped glass forming on its outer surface. The formation of glass film in the transition region on the outer surface of the porous layer can be accounted for by the fact that, during the consolidation process, heated gases move from a region heated to high temperature by a torch to lower temperature neighbouring regions and thus heat the porous layer in the transition region to the melting point of the material starting from its surface. It seems likely that a similar process takes place in the porous layer consolidation step during the FCVD preform fabrication process (as shown previously for the MCVD process [21]). In the transition region near the porous layer (Fig. 6c), the porous structure contains glassy regions differing in bismuth concentration: dark (0.05 at% Bi) and light (2.27 at% Bi). Figure 6d shows the transition region near the consolidated region. The glass resulting from the consolidation step is chemically inhomogeneous, as seen in Fig. 6f. In XRD patterns of different zones in the consolidated region, we found no evidence of crystalline phases. The luminescence of the sample under consideration was studied in two regions: in the consolidated region and in a narrow (~1 mm) transition region (Fig. 4a). The luminescence spectra obtained in the two regions were identical in shape. Figure 7 [spectra (*1, 2*)] shows luminescence spectra of only the consolidated region.

The absorption spectrum of an ~60-μm-thick consolidated layer in the sample under consideration is presented in Fig. 8.
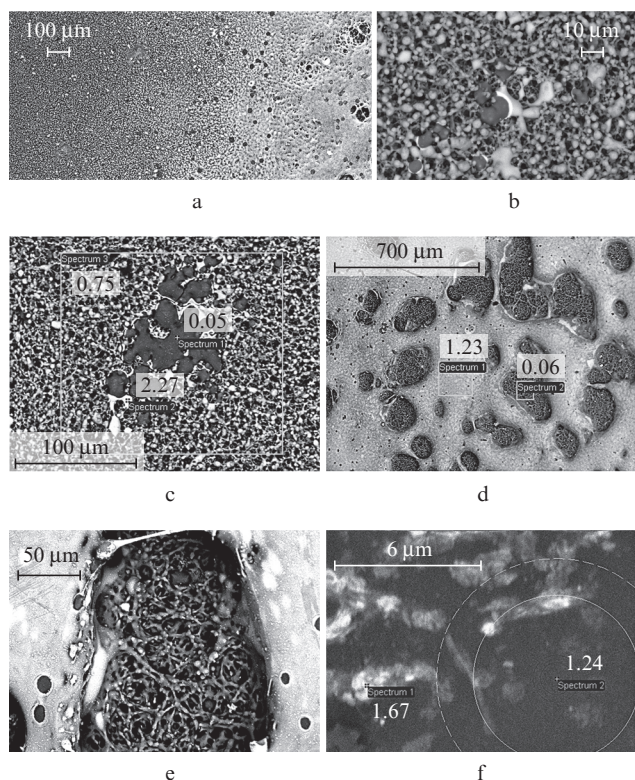
Figure 6. Backscatter-mode (*Z*-contrast) SEM micrographs of various regions of the sample represented in Fig. 4: (a) region of the porous layer (at left) and transition region (at right); (b) region of the porous layer; (c) formation of a glassy region (~100 μm in size) in the transition region (near the porous layer); (d) glass formation in the transition region (near the consolidated region); (e) higher magnification image of one of the 'craters' seen in panel d; (f) consolidated region.
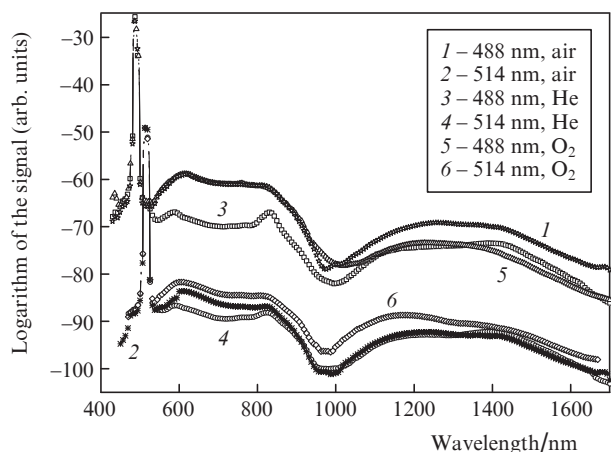

Figure 7. Luminescence spectra of layers consolidated in (*1, 2*) air (sample represented in Fig. 4a, three impregnation cycles), (*3, 4*) helium (one impregnation cycle) and (*5, 6*) oxygen (one impregnation cycle). For convenience of shape comparison, the spectra are offset along the vertical axis to bring the scattered pump peaks in coincidence.

The spectrum contains strong, broad absorption bands peaking at 222 and 290 nm and the edge of an even stronger absorption band at wavelengths under 210 nm.

Porous layer consolidation in a neutral (helium) and an oxidising (oxygen) atmosphere. Samples were impregnated with a 5 % $BiCl_3$ solution in acetone. After solvent vaporisa-
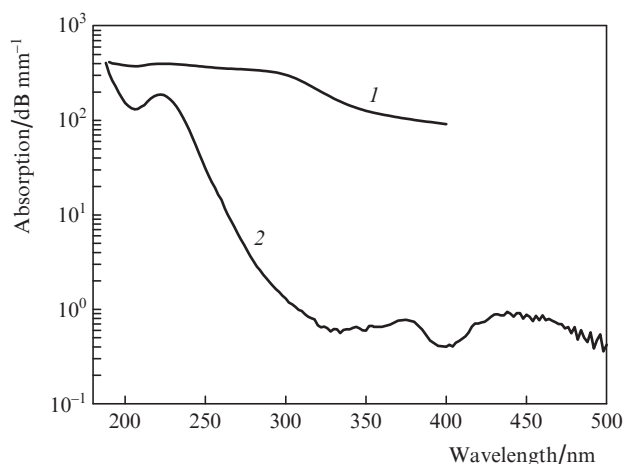

Figure 8. Absorption spectra of (*1*) a layer consolidated in air and (*2*) the zsBi preform (see Section 4).

tion, the samples were consolidated in a neutral (helium) or oxidising (oxygen) atmosphere. Figure 7 [spectra (*3–6*)] shows the luminescence spectra of the resultant layers. It is seen that the relative intensities of the luminescence bands depend slightly on the consolidation atmosphere. In particular, the sample consolidated in a helium atmosphere has slightly more prominent bands around 830 and 1420 nm than does the sample consolidated in air, and the sample consolidated in an oxygen atmosphere has a stronger band around 1150 nm. On the whole, however, the luminescence spectra of the samples differ little. No crystalline bismuth compounds were detected in these samples.

4. Characterisation of a bismuth-doped silica fibre preform free of other dopants

A fibre preform was fabricated by the FCVD process in combination with porous layer impregnation with a bismuth chloride solution in acetone (like in a previous study [17]). The porous layer (~300 μm in thickness) was impregnated three times with a 5 % $BiCl_3$ solution in acetone and dried after each impregnation cycle. Next, the porous layer was consolidated in an oxygen atmosphere at 1900 °C (the thickness of the sintered layer was ~60 μm). Immediately after the porous layer consolidation, the tube was shrunk to a smaller diameter, which was also done in an oxygen atmosphere (at 2000 °C). In the final step, the gas flow through the tube was shut off (but the tube remained filled with oxygen delivered previously) and the tube was collapsed at 2100 °C into a preform. Figure 9 shows a cross-sectional photograph and SEM image of the preform (denoted as zsBi). The diameter of its core (bismuth-doped region) is ~1.6 mm.

The highest bismuth concentration in the zsBi preform was about 0.03 at% as determined by X-ray microanalysis. (This value is approximate because it only slightly exceeds the detection limit of the method: 0.02 at%.) With allowance for porosity (~80 %), the bismuth content of the impregnated porous layer is ~1.2 at%. Thus, most of the bismuth vaporises during porous layer consolidation, tube contraction and tube collapse (~1/40 of the bismuth introduced into the porous layer remains in the core glass). Clearly, such losses make it difficult to fabricate fibres with controlled optical properties and ensure reproducibility of bismuth-doped fibres (the tendency of bismuth to vaporise in the fibre preform
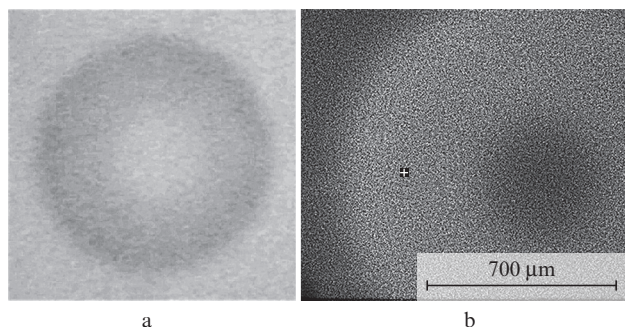
Figure 9. (a) Photograph (white light illumination) and (b) SEM image of the core of the zsBi preform (1-mm-thick disc-shaped sample). The highest measured bismuth concentration is about 0.03 at% (at the point marked by a cross).

fabrication process was also mentioned in previous studies [22–24]).

The UV absorption spectrum of the preform is presented in Fig. 8 [spectrum (2)]. Like the absorption spectrum of the porous layer [Fig. 8, spectrum (1)], it contains a strong band around 222 nm and an absorption edge at $\lambda < 210$ nm, but there is no band at 290 nm. In addition, the spectrum has bands peaking at 380 and 440 nm. It is worth noting that the marked difference between the absorption spectra of the porous layer and preform can be accounted for by the formation of metallic bismuth nanoparticles or bismuth chloride complexes (chlorobismuthates) in the consolidated layer. XRD examination detected no metallic bismuth nanoparticles in the layer (probably because of the very small particle size), but the observed high background absorption level can be interpreted as evidence for the presence of such particles in the glass [18]. The formation of chlorobismuthates in the glass also seems quite plausible given that chlorine is a major unintentional impurity (at a level of ~0.1% [25, 26]) in the FCVD and MCVD processes and that doping with the use of a bismuth chloride solution may further increase the chlorine concentration. The spectroscopic properties of such complexes in solutions containing ~15 ppm bismuth were reported in Refs [27–29]. It is of interest to note that the absorption bands of the consolidated glass at 222 and 290 nm are identical in position to those of Bi^{3+} and $BiCl_3$. That the absorption spectrum of the preform has no band at 290 nm can be interpreted as evidence that the $BiCl_3$ vaporises or decomposes in the tube collapse process.

Figure 10 shows luminescence spectra of the zsBi preform at different excitation wavelengths. The spectra are seen to comprise two broad, composite bands in the ranges 500–1000 and 1000–1700 nm. At the same time, the spectra obtained at excitation wavelengths of 647, 676 and 1330 nm contain relatively narrow (~100 nm) bands near 855, 830 and 1410 nm, respectively. In the range 500–1000 nm, there are at least three major bands: near 600, 720 and 830 nm. The band near 720 nm is hardly discernible, but the decomposition of the luminescence spectrum into Gaussian components ensures acceptable quality only when the number of components is at least three. In addition, there is a prominent shoulder near 910 nm. The peaks near 600 and 830 nm are due to Bi^{2+} and IRBCs, respectively [30]. The origin of the band near 720 nm is unclear. The luminescence band in the range 1000–1700 nm also comprises several components. In this range, at least two peaks can be identified: at 1240 and 1425 nm.
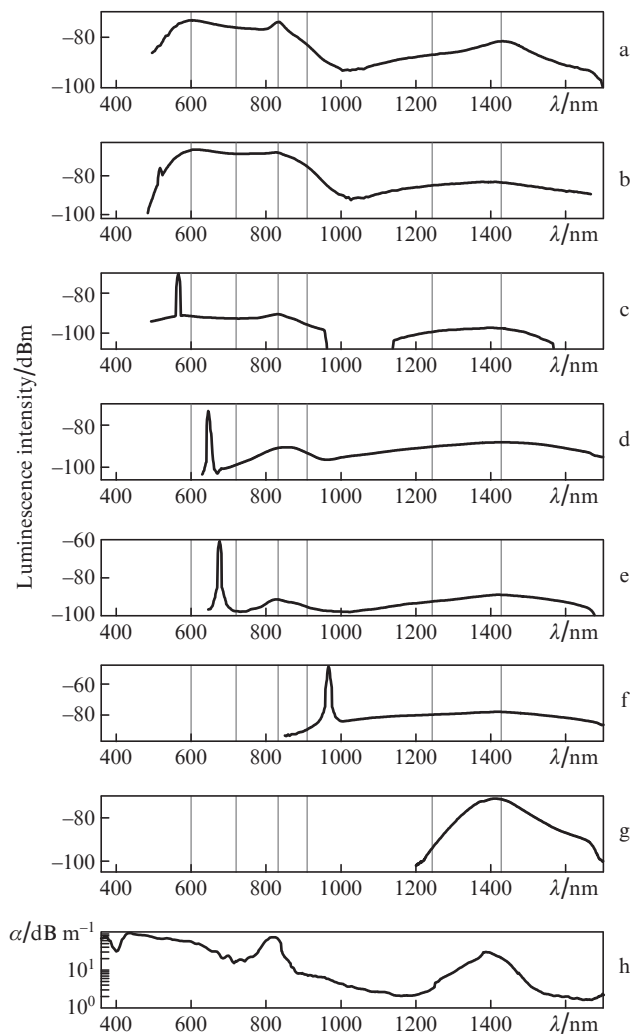

Figure 10. Luminescence spectra of the zsBi preform at excitation wavelengths λ_{ex} = (a) 337, (b) 514, (c) 568, (d) 647, (e) 676 and (f) 975 nm. The luminescence spectrum under excitation at λ_{ex} = 1330 nm (g) and the absorption spectrum (h) were obtained for an sBi fibre [17].

Figure 11 shows refractive index, calculated bismuth concentration, absorption and luminescence profiles across the zsBi preform. The refractive index profile (RIP) was measured in radial direction of the preform using a York Technology P102 preform analyser, with a resolution of 5 μm in the preform radius and ~0.0001 in the refractive index. The core diameter evaluated from the RIP was 1.6 mm. The bismuth concentration was assessed from the RIP using the relation $\Delta n / C_{Bi} \approx 0.015$ (at%)$^{-1}$ [22]. The bismuth concentration is taken to be zero at the point where the radial coordinate is $r = 0$. It is seen that the refractive index at $r = 0$ differs from that at $r > 0.8$ mm. One possible reason for this is that the synthetic silica glass of the Heraeus Suprasil F300 substrate tube had a higher chlorine concentration in comparison with the central part of the preform, where it was almost zero [25].

The absorption and luminescence profiles were measured on cross sections of the preform 0.04 and 1 mm in thickness (Fig. 11). The luminescence was excited at 337 nm, the laser beam was focused to a spot diameter of ~50 μm, and the sample was moved in 100-μm steps. In absorption profile measurements, a monochromatic probe beam was apertured by a rectangular slit 50×200 μm in dimensions. With allowance for
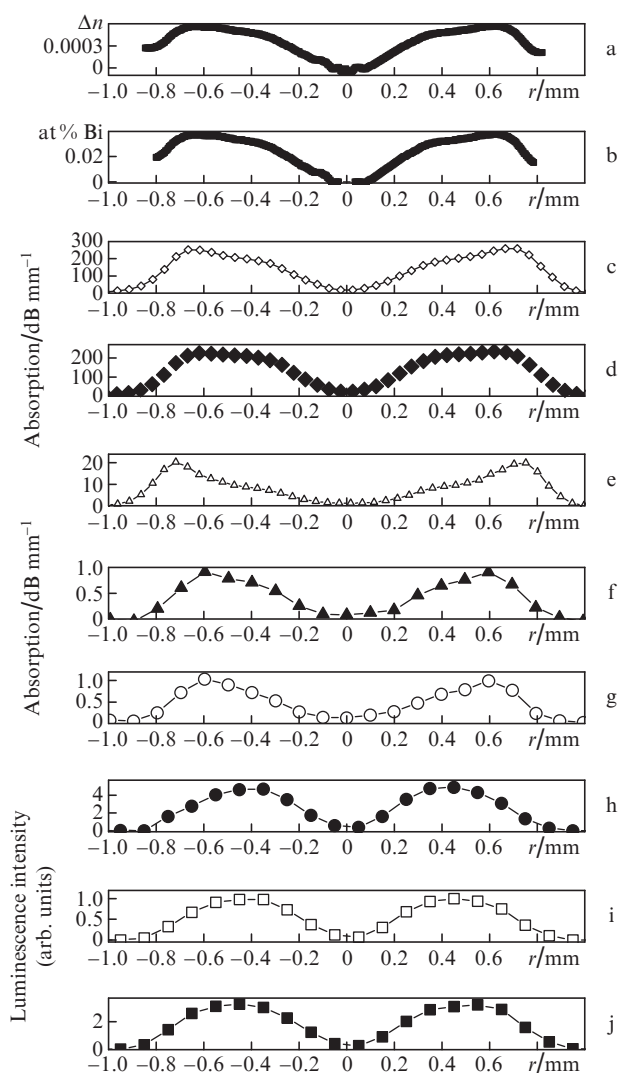
Figure 11. Refractive index profile ($\Delta n = n_{core} - n_{clad}$) (a); bismuth concentration profile extracted from the RIP (b); absorption profiles at λ_{abs} = 198 (c), 222 (d), 258 (e), 380 (f) and 440 nm (g); and luminescence profiles (λ_{ex} = 337 nm) at λ_{em} = 600 (h), 720 (i) and 830 (j). The error of determination does not exceed the size of the symbols.

the divergence of the probe beam over the sample thickness, the spatial resolution of the absorption profiles was ~150 µm.

As seen in Fig. 11, the 222-nm absorption profile is the most similar in shape to the RIP. The absorption band in the range 210–230 nm is present in spectra of many bismuth-containing materials and is commonly assigned to Bi^{3+} [27–29, 31–39]. On the other hand, the main bismuth oxide is Bi_2O_3, which contains bismuth in the form Bi^{3+}. Therefore, the observed similarity between the profiles in question suggests that the variation in the refractive index of the glass is due to bismuth in the oxidation stated 3+. These inferences are indirectly supported by EPR data for the preform. Since we failed to detect any EPR signal from bismuth (for example, from Bi^+, Bi^{2+} or Bi^{4+}), like in previous studies [40–43], it seems likely that the bismuth in the glass is predominantly in a nonparamagnetic state, such as Bi^{3+}. IRBCs result from the reduction of bismuth (as evidenced by a number of studies (see e.g. Refs [17, 18, 44–46]) and experimental data below) and obviously account for only a small percentage of the total bismuth concentration.

Another group of similar profiles is constituted by the 380- and 440-nm absorption profiles (the peak absorption wavelengths in Fig. 8). The corresponding bands are close in spectral position and consist of several components [15], so the similarity of the absorption profiles under consideration suggests that these bands are due to centres similar in nature or origin.

A third group of similar profiles comprises the radial profiles of the 600-, 720- and 830-nm luminescence intensity. The 600-nm band is known to arise from divalent bismuth, and the 830-nm band is due to IRBCs [30], but the similarity between the luminescence profiles corresponding to these bands suggests that such centres form in one or at least closely interrelated processes (which lead as well to the formation of the centre responsible for the luminescence band near 720 nm). Since visible and IR luminescence centres result from bismuth reduction [17], the luminescence profiles indicate a region where the bismuth is in a reduced state. It is worth noting that, in spite of the marked similarity between the luminescence profiles, the radial position of their maximum varies from 0.4 (luminescence near 600 nm) to 0.5 mm (luminescence near 830 nm).

Finally, the 258-nm absorption profile differs most significantly from all the other profiles in that it is dominated by the peak near the core–cladding interface. The specific shape of this profile points to a contribution from bismuth centres other than Bi^{3+}, Bi^{2+} and IRBCs and may be due to a strong effect of the tail of the absorption band peaking near 5 eV (248 nm), which arises from metallic bismuth nanoparticles in silica glass [47, 48]. Thus, the profile in Fig. 11e may represent the distribution of metallic bismuth nanoparticles over the zsBi preform. The maxima in this profile are located most closely to the interface between the doped core and silica glass cladding and correlate with the maximum in oxygen deficiency that would be expected in this region of the core (for example, by analogy with the position of germanium-related oxygen-deficient centres (ODCs) in germanosilicate preforms fabricated by the MCVD process [25, 49]).

Consider in greater detail preform fabrication by the FCVD process. Initially, after prolonged porous layer impregnation with a $BiCl_3$ solution in acetone, the bismuth is uniformly distributed across the porous layer, which consists of submicron-sized particles and CH_3–C(O)–CH_3·$BiCl_3$ on their surface. In the porous layer consolidation process in flowing oxygen, the temperature is raised to 1900 °C. Since oxygen is a stronger oxidant than is $BiCl_3$, it is reasonable to assume that the hydrocarbon component of CH_3–C(O)–CH_3·$BiCl_3$ burns to give carbon dioxide and water, and that $BiCl_3$ oxidises to form Bi_2O_3 and Cl_2 (Cl_2 evolution is evidenced by the fact that, during porous layer consolidation, a yellow-green gas appears in the substrate tube). The oxidation of $BiCl_3$ seems to follow the reaction schemes [50] $2 BiCl_3 + O_2 = 2 Bi(Cl)O + 2 Cl_2$ (formation of bismuth oxychloride in the temperature range 250–350 °C) and $3 Bi(Cl)O = Bi_2O_3 + BiCl_3$ (formation of bismuth oxide in the temperature range 575–600 °C).

The melting and boiling points of these compounds are indicated in Table 1 [50]. Clearly, bismuth in oxide form prevails at 1900 °C. At this temperature, vaporisation of bismuth oxide is accompanied by its decomposition according to the scheme $Bi_2O_3 = 2 Bi + 1.5 O_2$. In particular, Bi, Bi_2 and O_2 account for 85% of the gas phase over bismuth oxide even at $T = 890$ °C, whereas the fraction of Bi_2O_3 monomers and dimers is just 5% [51]. Bi_2O_3 decomposition in the porous layer consolidation process is further evidenced by the forma-

Table 1. Melting and boiling points of bismuth compounds.

Substance	T_m/°C	T_b/°C	Decomposition upon vaporisation
BiCl$_3$	232	441	Not known
Bi(Cl)O	232.5	–	Not known
Bi$_2$O$_3$	825	1890	Bi, Bi$_2$, O$_2$, Bi$_2$O$_3$, Bi$_4$O$_6$ [51]
Metallic bismuth	271.44	1564	–

tion of metallic bismuth crystals (Fig. 5) in the blackened porous layer (Fig. 4a). Thus, the gas phase forming in the porous layer and consisting largely of Bi, Bi$_2$, O$_2$ and Cl$_2$ atoms and molecules leaves it and enters the gas (oxygen or helium) flow along the tube, diffusing through a relatively large thickness of the porous layer (several thousand layers of SiO$_2$ particles). A portion of the bismuth, proportional to its concentration in the gas phase, is captured by the surface of the SiO$_2$ particles and dissolves in the silica. Therefore, the bismuth concentration should increase with increasing distance from the porous layer surface exposed to oxygen (i.e. as the surface of the substrate tube is approached). The region $0.3 < r < 0.7$ mm in the preform is consistent with this model (Figs 11a, 11b, 11d).

To explain the more rapid drop in bismuth concentration and, hence, in refractive index in the region $0 < r < 0.3$ mm and the shift of the maximum in the luminescence profiles towards the centre of the preform, we take into account that the bismuth oxide dissolved in the glass matrix in the consolidation step also seems to have a tendency to dissociate into bismuth and oxygen during heating in the tube collapse process, with subsequent outdiffusion of the dissociation products from the consolidated layer. However, since the diffusion coefficient of bismuth is smaller than that of oxygen, the bismuth-deficient region is smaller ($0 < r < 0.3$ mm as follows from the RIP) than the oxygen-deficient region ($0.3 < r < 0.7$ as follows from the luminescence profiles). This model accounts for the radial distributions presented in Fig. 11 and is consistent with the conclusion that the RIP is determined by Bi^{3+}, whereas the luminescence profiles are determined by bismuth in a lower oxidation state (subvalent bismuth). Previously, similar processes were assumed to be responsible for the increased concentration of germanium-related ODCs in the central and peripheral parts of MCVD germanosilicate glass preforms [25, 49].

Crucial for validating the above model is the concentration of 'free' oxygen, capable of readily diffusing, in the bismuth-doped glass: it should exceed the concentration corresponding to oxygen solubility at a given temperature and oxygen pressure in the ambient atmosphere. Free oxygen results from bismuth oxide dissociation and its concentration is of the same order as the atomic concentration of bismuth (there are 3/4 of an oxygen molecule per bismuth atom) because SiO$_2$ dissociation can be neglected [51].

Complete bismuth oxide dissociation in the zsBi preform, containing 0.03 at% bismuth, at $T = 2000-2100$ °C would correspond to a free oxygen concentration in the glass of $\sim 1.5 \times 10^{19}$ cm^{-3}. Oxygen solubility in silica glass at temperatures from 950 to 1100 °C is known to be $\sim 2 \times 10^{-3}$, i.e. the equilibrium oxygen concentration in glass is about 500 times lower than the concentration of molecules in the ambient oxygen atmosphere [52]. The solubility of gases in glass typically varies little with temperature [53], so the above value can be used as well for ~ 2000 °C.

Since the oxygen concentration in the tube in the collapse process at a pressure near 1 atm and a temperature $T = 2100$ °C is $\sim 3.3 \times 10^{18}$ cm^{-3}, the corresponding equilibrium concentration of oxygen dissolved in glass is 6.6×10^{15} cm^{-3}. Comparison of this value with the concentration of oxygen bonded to bismuth indicates that dissociation of just $\sim 1/2000$ of the bismuth oxide is sufficient for creating reducing conditions for bismuth. Thus, oxygen outdiffusion from the glass and, accordingly, reducing conditions for bismuth in this step of the fabrication process can be ensured even in an oxygen atmosphere. The shift of the maxima in the luminescence profiles towards the centre of the preform with respect to the bismuth concentration profile is also consistent with the oxygen diffusion hypothesis given that luminescence profiles are proportional, among other things, to the free oxygen deficiency profile.

5. Effect of annealing under oxidising and reducing conditions on the spectroscopic properties of Bi:SiO$_2$ fibres

The zsBi preform was drawn into two holey fibres (with holes around their core). Some properties of such fibres were reported previously [17]. The atmosphere in the holes during the fibre drawing process at a temperature of 1850 °C (slightly below the porous layer consolidation temperature) had a significant effect on the luminescence characteristics of the fibres. The fibre whose holes were filled with flowing oxygen during drawing (denoted as sBiO in what follows) showed no luminescence. The fibre whose holes were filled with flowing argon during drawing (denoted as sBiAr in what follows) showed both IR and visible luminescence. The apparent contradiction with the effect of the atmosphere in the tube collapse step can probably be resolved by taking into account the difference in temperature (2100 and 1850 °C) and oxygen pressure (1 and 1.3 atm) between the collapse and drawing processes. Moreover, the extent of Bi$_2$O$_3$ dissociation is smaller at a lower temperature and, hence, the free oxygen concentration in the fibre is substantially lower than that in the preform.
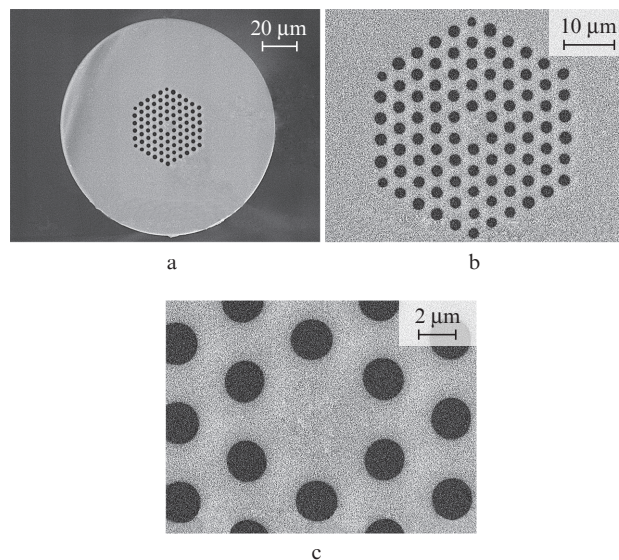
Figure 12. SEM images of the sBiO fibre end face.

The sBiAr fibre was studied previously [17]. Here we focus on the sBiO fibre. Figure 12 shows SEM images of the sBiO fibre end face. This fibre was produced by drawing an assembly of capillaries and a zsBi preform core rod and simultaneously overcladding the assembly with a jacketing tube during drawing.
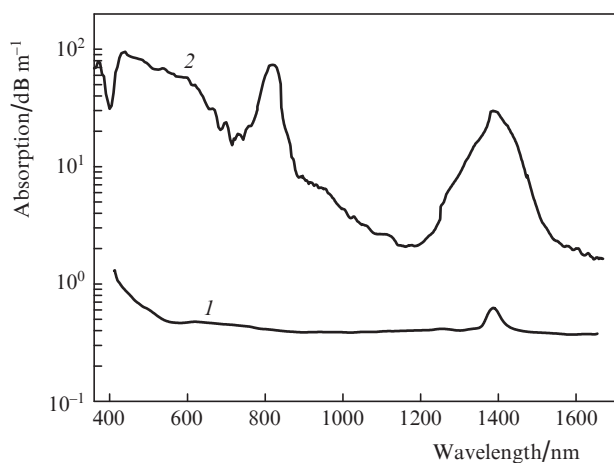

Figure 13. Absorption spectra of the (*1*) sBiO and (*2*) sBiAr [17] fibres.

Figure 13 presents the loss spectra of the sBiO and sBiAr fibres. It is seen that drawing with oxygen in the holes eliminates the absorption bands of IRBCs. The absorption edge of the sBiO fibre in the range $\lambda < 500$ nm seems to be due to Bi^{3+}.

Figure 14 shows the spectral dependences of the absorption induced in the sBiO fibre during heating with oxygen in its holes (the experimental configuration was reported elsewhere [18]). With increasing temperature, the absorption increases monotonically throughout the spectral region studied. The opposite is observed during cooling: the absorption decreases with decreasing temperature. After annealing, the fibre also showed no visible or IR luminescence. An attempt to interpret the background loss in terms of an Urbach-like edge in the short-wavelength spectral region was unsuccessful because the measured spectra considerably deviated from
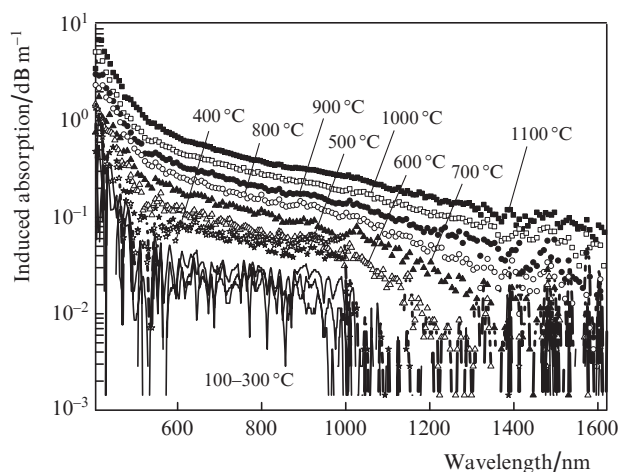
Urbach's rule behaviour (exponential variation of the absorption coefficient with frequency) [54]. Additional work is necessary to clarify the mechanism of this absorption.

Figure 15 shows spectra of the absorption induced in the sBiO fibre during heating with argon in its holes. The absorption increased more significantly in comparison with oxygen annealing and remained unchanged during cooling. The spectra clearly demonstrate the formation and growth of absorption bands peaking at 820 and 1400 nm, characteristic of IRBCs. The formation of IRBCs was further supported by the fact that the fibre exhibited luminescence after cooling to room temperature.
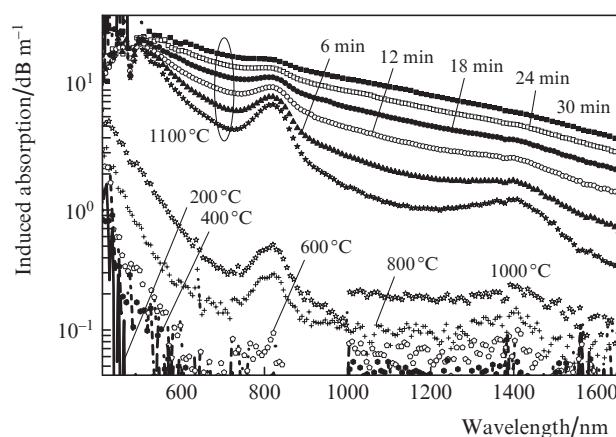

Figure 15. Induced absorption in the sBiO fibre after heating with argon in its holes.

This experiment, carried out under reducing conditions, provides further evidence that IRBCs are due to bismuth in a low oxidation state. During subsequent holding of the fibre at a temperature of 1100 °C for 30 min, the strength of the absorption bands at 820 and 1400 nm decreased (Fig. 15). The background loss increased throughout the reduction process. The background loss was studied in detail elsewhere [18] and seems to arise from the absorption in metallic bismuth nanoparticles.

6. Conclusions

The present results lead us to the following conclusions:

1. The behaviour of bismuth in various steps of the fabrication of $Bi:SiO_2$ core fibres by the FCVD process (bismuth chloride, bismuth chloride solution in acetone, porous layer impregnated with the solution, consolidated layer, fibre preform and fibres drawn out in different gaseous atmospheres) has been investigated by spectroscopic techniques and X-ray diffraction.

2. Bi^{3+}, evidenced by the absorption band near 220 nm, is present in all the steps of the process.

3. Bi^{2+}, evidenced by the luminescence band around 600 nm, and the centre responsible for the luminescence band centred at 720 nm appear during porous layer consolidation and persist/disappear in subsequent steps together with IR luminescence.

4. IRBCs, evidenced by the absorption bands at 820 and 1400 nm and/or the luminescence bands around 830 and 1430 nm, appear during porous layer consolidation and persist/disappear in subsequent steps together with Bi^{2+}.

Figure 14. Induced absorption in the sBiO fibre after heating with oxygen in its holes.

5. The observed radial distributions of the refractive index, absorption and luminescence in the fibre preforms have been interpreted in terms of bismuth oxide (Bi_2O_3) dissociation and subsequent diffusion of the dissociation products (Bi and O/O_2). The dissociated oxygen concentration can exceed oxygen solubility in silica glass at an external oxygen pressure of 1 atm, i.e. even in an oxygen atmosphere the porous layer consolidation and tube collapse processes may correspond to reducing conditions for bismuth present in the glass network.

6. The present results indicate that, after tube collapse in oxygen at atmospheric pressure, the bismuth in the $Bi:SiO_2$ (~ 0.03 at% Bi) preform is predominantly in the oxidation state 3+ and that it is the bismuth in this oxidation state which is responsible for the increased refractive index of the core glass in the preform. An increase in the total bismuth concentration in the glass or heat treatment under reducing conditions leads to the formation of metallic bismuth nanoparticles.

7. Depending on the atmosphere in the holes of preforms and fibres during fibre drawing ($T \approx 2000\,°C$) and annealing ($T = 1100\,°C$), one can create reducing or oxidising conditions for bismuth, resulting in or suppressing IRBC luminescence, respectively.

8. Annealing the fibres under reducing conditions produces IRBC-related absorption bands and concurrently increases the background loss, irreversible on cooling. During annealing in argon atmosphere at $T_{max} = 1100\,°C$ for 30 min, the IRBC concentration passes through a maximum and then decreases, whereas the background loss increases monotonically.

References

1. Dianov E.M., Dvoyrin V.V., Mashinsky V.M., Umnikov A.A., Yashkov M.V., Gur'yanov A.N. *Kvantovaya Elektron.*, **35**, 1083 (2005) [*Quantum Electron.*, **35**, 1083 (2005)].

2. Razdobreev I., Bigot L., Pureur V., Favre A., Bouwmans G., Douay M. *Appl. Phys. Lett.*, **90**, 031103 (2007).

3. Kalita M.P., Yoo S., Sahu J. *Opt. Express*, **16**, 21032 (2008).

4. Dianov E.M., Firstov S.V., Khopin V.F., Gur'yanov A.N., Bufetov I.A. *Kvantovaya Elektron.*, **38**, 615 (2008) [*Quantum Electron.*, **38**, 615 (2008)].

5. Bufetov I.A., Dianov E.M. *Laser Phys. Lett.*, **6**, 487 (2009).

6. Dvoyrin V.V., Medvedkov O.I., Mashinsky V.M., Umnikov A.A., Guryanov A.N., Dianov E.M. *Opt. Express*, **16**, 16971 (2008).

7. Bufetov I.A., Shubin A.V., Firstov S.V., Medvedkov O.I., Melkumov M.A., Khopin V.F., Guryanov A.N., Dianov E.M. in *37th Europ. Conf. and Exp. on Optical Communications, OSA Technical Digest (CD)* (OSA, 2011) paper Tu.3.LeCervin.3.

8. Melkumov M.A., Bufetov I.A., Shubin A.V., Firstov S.V., Khopin V.F., Guryanov A.N., Dianov E.M. *Opt. Lett.*, **36**, 2408 (2011).

9. Peng M., Dong G., Wondraczek L., Zhang L., Zhang N., Qiu J. *J. Non-Cryst. Solids*, **357**, 2241 (2011).

10. Malinin A.A., Zlenko A.S., Akhmetshin U.G., Semjonov S.L. *Proc. SPIE Int. Soc. Opt. Eng.*, **7934**, 793418 (2011).

11. Giraud A., Sandoz F., Pelkonen J. *Proc. 14th OptoElectronics and Communications Conf.* (Hong Kong, 2009) p. 1.

12. Neff M., Romano V., Luthy W. *Opt. Mater.*, **31**, 247 (2008).

13. Razdobreev I., El Hamzaoui H., Ivanov V.Yu., Kustov E.F., Capoen B., Bouazaoui M. *Opt. Lett.*, **35**, 1341 (2010).

14. Bufetov I.A., Semenov S.L., Vel'miskin V.V., Firstov S.V., Bufetova G.A., Dianov E.M. *Kvantovaya Elektron.*, **40**, 639 (2010) [*Quantum Electron.*, **40**, 639 (2010)].

15. Razdobreev I., El Hamzaoui H., Bigot L., Arion V., Bouwmans G., Le Rouge A., Bouazaoui M. *Opt. Express*, **18**, 19479 (2010).

16. Bufetov I.A., Melkumov M.A., Firstov S.V., Shubin A.V., Semenov S.L., Vel'miskin V.V., Levchenko A.E., Firstova E.G., Dianov E.M. *Opt. Lett.*, **36**, 166 (2011).

17. Zlenko A.S., Dvoyrin V.V., Mashinsky V.M., Denisov A.N., Iskhakova L.D., Mayorova M.S., Medvedkov O.I., Semenov S.L., Vasiliev S.A., Dianov E.M. *Opt. Lett.*, **36**, 2599 (2011).

18. Zlenko A.S., Mashinsky V.M., Iskhakova L.D., Semjonov S.L., Koltashev V.V., Karatun N.M., Dianov E.M. *Opt. Express*, **20**, 23186 (2012).

19. Samuel R. *Rev. Mod. Phys.*, **18**, 103 (1946).

20. Sanderson J., Bayse C.A. *Tetrahedron*, **64**, 7685 (2008).

21. Kozlova M.A., Kornev V.V., Luzhain V.G. *Izv. Akad. Nauk SSSR, Neorg. Mater.*, **19**, 321 (1983).

22. Dvoyrin V.V., Mashinsky V.M., Bulatov L.I., Bufetov I.A., Shubin A.V., Melkumov M.A., Kustov E.F., Dianov E.M., Umnikov A.A., Khopin V.F., Yashkov M.V., Guryanov A.N. *Opt. Lett.*, **31**, 2966 (2006).

23. Umnikov A.A., Guryanov A.N., Abramov A.N., Vechkanov N.N., Firstov S.V., Mashinsky V.M., Dvoyrin V.V., Bulatov L.I., Dianov E.M. in *34th Europ. Conf. on Optical Communication* (Brussels, 2008).

24. Zlenko A.S., Akhmetshin U.G., Dvoyrin V.V., Bogatyrev V.A., Firstov S.V. *Kvantovaya Elektron.*, **39**, 1071 (2009) [*Quantum Electron.*, **39**, 1071 (2009)].

25. Gur'yanov A.N., Dianov E.M., Lavrishchev S.V., Mazavin S.M., Mashinsky V.M., Neustruev V.B., Sokolov N.I., Khopin V.F. *Fiz. Khim. Stekla*, **12**, 359 (1986).

26. Hanafusa H., Tajima Y. *Electron. Lett.*, **20**, 178 (1984).

27. Newman L., Hume D.N. *J. Am. Chem. Soc.*, **79**, 4576 (1957).

28. Newman L., Hume D.N. *J. Am. Chem. Soc.*, **79**, 4581 (1957).

29. Kartuzhanskii A.L., Plachenov B.T., Sokolova I.V., Studzinskii O.P. *J. Appl. Spectrosc.*, **48**, 308 (1988).

30. Firstov S.V., Khopin V.F., Bufetov I.A., Firstova E.G., Guryanov A.N., Dianov E.M. *Opt. Express*, **19**, 19551 (2011).

31. Radhakrishna S., Srinivasa Setty R.S. *Phys. Rev. B*, **14**, 969 (1976).

32. Glasner A., Reisfeld R. *J. Chem. Phys.*, **32**, 956 (1960).

33. Merritt Ch. Jr., Hershenson H.M., Rogers L.B. *Anal. Chem.*, **25**, 572 (1953).

34. Zhiwu P., Qiang S., Jiyu Z. *Solid State Commun.*, **86**, 377 (1993).

35. Blasse G., Bril A. *J. Chem. Phys.*, **48**, 217 (1968).

36. Smith G.P., James D.W., Boston C.R. *J. Chem. Phys.*, **42**, 2249 (1965).

37. Pedrini C., Boulon G., Gaume-Mahn F. *Phys. Status Solidi A*, **15**, K15 (1973).

38. Eve A.J., Hume D.N. *Inorg. Chem.*, **3**, 276 (1964).

39. Bjerrum N.J., Boston C.R., Smith G.P. *Inorg. Chem.*, **6**, 1162 (1967).

40. Fujimoto Y., Nakatsuka M. *Jpn. J. Appl. Phys.*, **40**, L279 (2001).

41. Fujimoto Y. *J. Am. Ceram. Soc.*, **93**, 581 (2010).

42. Peng M.Y., Wang C., Chen D.P., Qiu J.R., Jiang X.W., Zhu C.S. *J. Non-Cryst. Solids*, **351**, 2388 (2005).

43. Peng M.Y., Wu B.T., Da N., Wang C., Chen D.P., Zhu C.S., Qiu J.R. *J. Non-Cryst. Solids*, **354**, 1221 (2008).

44. Khonthon S., Morimoto S., Arai Y., Ohishi Y., Suranaree J. *Sci. Technol.*, **14**, 141 (2007).

45. Denker B.I., Galagan B.I., Osiko V.V., Shulman I.L., Sverchkov S.E., Dianov E.M. *Appl. Phys. B*, **98**, 455 (2010).

46. Dvoretskii D.A., Bufetov I.A., Vel'miskin V.V., Zlenko A.S., Khopin V.F., Semjonov S.L., Gur'yanov A.N., Denisov L.K.,

Dianov E.M. *Kvantovaya Elektron.*, **42**, 762 (2012) [*Quantum Electron.*, **42**, 762 (2012)].

47. Park S.Y., Weeks R.A., Zuhr R. *J. Appl. Phys.*, **77**, 6100 (1995).

48. Pan Z., Morgan S.H., Henderson D.O., Park S.Y., Weeks R.A., Magruder R.H. III, Zuhr R.A. *Opt. Mater.*, **4**, 675 (1995).

49. Dianov E.M., Mashinsky V.M., Neustruev V.B., Sazhin O.D., Guryanov A.N., Khopin V.F., Vechkanov N.N., Lavrishchev S.V. *Opt. Fiber Technol.*, **3**, 77 (1997).

50. Lidin R.A., Andreeva L.L., Molochko V.A. *Constants of Inorganic Substances: A Handbook* (New York: Begell House, 1995).

51. Kazenas E.K., Tsvetkov Yu.V. *Isparenie oksidov* (Vaporisation of Oxides) (Moscow: Nauka, 1997) p. 210.

52. Norton F.J. *Nature*, **191**, 701 (1961).

53. Shackelford J.F. *J. Non-Cryst. Solids*, **253**, 231 (1999).

54. Dow J., Redfield D. *Phys. Rev. B*, **5**, 594 (1972).